Available online at www.sciencedirect.com
ScienceDirect
International Journal of Thermal Sciences 46 (2007) 385–398
International Journal of Thermal Sciences
www.elsevier.com/locate/ijts

Laser heating: jet emanating from laser induced cavity

B.S. Yilbas *, S.B. Mansour

KFUPM Box 1913, Dhahran 31261, Saudi Arabia

Received 18 February 2006; received in revised form 13 April 2006; accepted 17 June 2006

Available online 22 August 2006

Abstract

Laser heating of steel surface and cavity formation during laser irradiation pulse are investigated. The recession of the solid surface due to melting and evaporation is modeled using an energy method. Jet emerging from the laser induced cavity and expanding into stagnant water, resembling laser shock processing, is also simulated. Governing flow equations are solved numerically using a control volume approach employing a moving mesh in the solution domain. This is because of the recessing surfaces of the vapor, liquid and solid phases during the heating pulse. It is found that mushy zone size at liquid–vapor interface is larger than that of at solid–liquid interface. Expansion of the vapor jet, emanating from the cavity and expanding into stagnant water ambient, is high in the axial direction in the early heating period, and as the time progresses the radial expansion of the jet becomes visible due to pressure build up in the jet frontal area. Considerably high recoil pressure is developed in the cavity due to high recession velocity of cavity surface and expansion velocity of vapor jet.

Keywords: Laser; Heating; Cavity; Vapor; Jet; Expansion

1. Introduction

In some machining situations, thermal processing of materials in industry offers advantages over the mechanical processing such as traditional machining. One of thermal machining process is laser machining, which offers low cost, precision of operation, and short processing time. Laser machining is involved with phase change processes; in which case, substrate material is heated to the melting temperature, then, phase changes including melting and consequent evaporation are resulted. Since the process is rapid, particularly for short pulse processing, experimentation of the physical processes during laser–solid interaction is difficult and becomes costly. However, model studies provide information on the physical processes, which take place during the laser workpiece interaction, with parametric variation. Consequently investigation into such physical processes becomes essential for advancement in laser machining operation.

Considerable research studies were carried out to examine laser heating process in relation to machining. Laser induced vaporization and material removal from solid targets were studied by Dabby and Peak [1]. They formulated the evaporation process analytically by assuming constant recession velocity of the solid surface. Yilbas et al. [2] formulated analytically laser machining process and evaporation of the surface. Their results were in agreement with the experimental findings for millisecond laser pulses. Energy transfer and penetration velocity during a high-energy drilling process were investigated by Wei and Ho [3]. They indicated that a conventional one-dimensional evaporation model was inherently invalid due to a significant overestimation of the evaporation rate. A key-hole formation during laser irradiation pulse was examined by Tix and Simon [4]. They formulated the evaporated front behavior after considering the plasma formation in the vapor phase. Conduction and advection heat transfer in solid and liquid metal during laser heating were formulated by Ganesh et al. [5]. They introduced a numerical method to determine liquid and vapor properties. The recoil pressure generation during laser heating of surface was examined by Semak and Matsunawa [6]. They indicated that the convection term in the energy equation for modeling of key-hole formation should not be omitted, since it had significant effect on the heat transfer rates. A mathematical model for the laser drilling process due to laser pulse irradia-

* Corresponding author.
E-mail address: bsyilbas@kfupm.edu.sa (B.S. Yilbas).

1290-0729/$ – see front matter
doi:10.1016/j.ijthermalsci.2006.06.013

Nomenclature

a	Gaussian parameter	m
A	area	m^2
a	Gaussian parameter	m
Cp	specific heat capacity	$J\,kg^{-1}\,K^{-1}$
C	various empirical constants in turbulence model	
$cp_{1,2,3,4,5}$	coefficients in the source term	
D	species diffusion coefficient	$m^2\,s^{-1}$
	jet width	m
$f(r,t)$	cavity profile equation	
h	convective heat transfer coefficient	$W\,m^{-2}\,K^{-1}$
	sensible enthalpy	$J\,kg^{-1}$
I_o	laser power intensity	$W\,m^{-2}$
J_j	total flux (convection plus diffusion) across face 'j'	$kg\,s^{-1}m^{-2} \times [\phi]$
K	turbulence kinetic energy	$m^2\,s^{-2}$
k	thermal conductivity	$W\,m^{-1}\,K^{-1}$
k_t	turbulent thermal conductivity	$W\,m^{-1}\,K^{-1}$
L	latent heat	$J\,kg^{-1}$
Pr	Prandtl number	
$\bar{p}$	time-averaged pressure	Pa
p'	fluctuating component of mixture pressure	Pa
$\bar{p}'$	pressure correction	Pa
r	distance along the radial direction	m
r_f	reflectance	
S	source term	$W\,m^{-3}$
Sc	Schmidt number	
T	temperature	K
$\bar{T}$	time-averaged temperature	K
T'	fluctuating component of temperature	K
t	time	s
t_m	time at which melting starts in the solid phase	s
t_{sl}	time at which solid–liquid mushy zone starts converting into the liquid phase	s
t_b	time at which evaporation starts in the liquid phase	s
U	energy content	J
u	velocity component	$m\,s^{-1}$
	z-direction velocity	$m\,s^{-1}$
$\bar{u}$	time-averaged velocity component	$m\,s^{-1}$
	time-averaged z-direction velocity	$m\,s^{-1}$
u'	fluctuating component of z-direction velocity	$m\,s^{-1}$
$\bar{u}'$	z-direction velocity correction	$m\,s^{-1}$
$\bar{u}^*$	guessed z-direction velocity	$m\,s^{-1}$
$\forall$	volume	m^3
V	velocity	$m\,s^{-1}$
v	r-direction velocity	$m\,s^{-1}$
$\bar{v}$	time-averaged r-direction velocity	$m\,s^{-1}$
v'	fluctuating component of r-direction velocity	$m\,s^{-1}$
$\bar{v}'$	r-direction velocity correction	$m\,s^{-1}$
$\bar{v}^*$	guessed z-direction velocity	$m\,s^{-1}$
x	quality	
Y	mass fraction in species transport model	
$\bar{Y}$	time-averaged mass fraction in species transport model	
zc	depth of cavity	m
z	distance along the radial direction	m

Greek symbols

δ	reciprocal of absorption depth	m^{-1}
ε	rate of dissipation	$m^2\,s^{-3}$
Γ	diffusion coefficient	$kg\,m^{-1}\,s^{-1}$
μ	molecular viscosity coefficient	$kg\,m^{-1}\,s^{-1}$
μ_t	turbulent viscosity coefficient	$kg\,m^{-1}\,s^{-1}$
ϕ	arbitrary variable	
$[\phi]$	unit of arbitrary variable ϕ	
ρ	density	$kg\,m^{-3}$
$\bar{\rho}$	time-averaged density	$kg\,m^{-3}$
ρ'	fluctuating component of density	$kg\,m^{-3}$
σ_K	turbulent Prandtl number for K	
σ_ε	turbulent Prandtl number for ε	

Subscripts

b	vapour–liquid mushy zone; boiling
eff	effective
l	liquid
max	maximum; maximum cavity radius
m	solid–liquid mushy zone; melting
o	initial value
p	time index
ref	reference
s	solid, surface
t	turbulent
v	vapor

tion onto a solid surface was introduced by Solana et al. [7]. They indicated that liquid ejection from the laser produced cavity should be considered for laser power intensities close to the threshold intensity for evaporation. Yilbas et al. [8] investigated laser induced phase change processes in relation to drilling. However, the studies were limited to vapor front formation and vapor front expansion into its ambient was omitted. In order to comprehend the examination of the laser–solid interaction, vapor front formation and its expansion into ambient should be accommodated in the analysis. When high intensity laser beam interacts with the solid surface, evaporation of the surface expands into its ambient. Through the momentum change across the vapor front and the recessing irradiated surface, a recoil pressure is generated. The magnitude of recoil pressure is mainly depended on the rate of vapor front expansion and pulse duration. In addition, the ambient of vapor front influences significantly depth of vapor front penetration and magnitude of recoil pressure. Since the physical processes last in short time period, measurement of front penetration depth and recoil pressure is difficult and being costly. Consequently, modeling and

simulation of vapor front penetration into its ambient and recoil pressure generation become essential.

Considerable research studies were carried out on jet expansion. Transient jet expansion into quiescent ambient was investigated numerically by Abraham [9]. He used k–ε model to account for the turbulence. He showed that entrainment rate was to scale linearly with axial penetration and total mass entrained had a cubic dependence on axial penetration of the jet. Transient turbulent gas jet injection in relation to diesel engine was studied by Ouellette and Hill [10]. They used k–ε turbulence model in the analysis and discussed the affecting parameters on jet expansion. The penetration depth and spreading rate of non-harmonic unsteady jet was examined by Kouros et al. [11]. They showed that the spreading rate remained nearly constant where as the velocity varied considerably during jet expansion. The flow characteristics of turbulent radial jet were examined experimentally by Witze and Dwyer [12]. They indicated that radial jet spread at a rate more than the plane jet. Development of transient jets and evolving of diffusion flames were investigated by Park and Shih [13]. They indicated that the normalized jet width in the evolving jet diffusion flame was constant in the flow down stream. Arshad et al. [14] investigated jet emanating from the surface resembling the laser produced vapor front. However, the study was limited with the helium jet and cavity formation during the laser-workpiece interaction was avoided. Yilbas et al. [15] measured a laser produced jet properties for microsecond heating durations. They indicated that jet has a parabolic velocity distribution in the vicinity of the cavity exit.

In the present study, laser evaporative heating of the solid surface is modeled. Cavity formation and mushy zones development at the interface of vapor–liquid and liquid–solid phases are predicted. The vapor front expansion and penetration into stagnant water is considered and flow properties of expanding front are predicted through solving governing flow equations. K–ε turbulence model is accommodated to account for the turbulence in the jet. Since the density of the vapor front (metal vapor) is not known and vary with mass removal rate from the cavity, two densities of vapor front are employed in the simulations. The selection of vapor density is based on the previous predictions [16]. In addition, it is assumed that the vapor front expands into stagnant water ambient. The selection of water ambient is due to resembling of laser shock processing; in which case, evaporating front ambient is either a dense layer, such as an overlay or water.

2. Heating analysis and transiently developing vapor jet simulation

Energy equation for each phase is solved independently as well as being coupled across the interfaces of the two-phases, where both phases exist mutually (mushy zones). The laser output power intensity distribution at the workpiece surface is considered being Gaussian and its centre is located at the centre of the co-ordinate system. The temporal variation of laser power intensity resembling the actual laser pulse is accommodated in the simulations. This arrangement results in an axisymmetric heating of the workpiece material. The heat conduction equation for a solid phase heating due to a laser irradiation pulse with a Gaussian intensity profile can be written as:

$$\rho_s c_{p_s} \frac{\partial T}{\partial t} = \frac{k_s}{r} \frac{\partial}{\partial r}\left(r \frac{\partial T}{\partial r}\right) + k_s \frac{\partial^2 T}{\partial z^2} + S_o \tag{1}$$

where S_o is the volumetric source term and it is,

$$S_o = I_o \delta (1 - r_f) \exp(-\delta z) \exp\left(-\frac{r^2}{a^2}\right) \tag{2}$$

I_o, δ, r_f and a are the laser peak power intensity, absorption coefficient, reflectivity and the Gaussian parameter, respectively.

The initial and boundary conditions for Eq. (1) are given below. Initially, the substrate material is assumed at a uniform temperature, T_o, i.e.:

At time zero $\Rightarrow$ $t = 0$: $T(r, z, 0) = T_o$ (specified)

At a distance considerably away from the surface (at infinity) in the radial direction a constant temperature T_o is assumed. Since the heating has no effect on the temperature rise at a depth of infinity below the surface, temperature is assumed to be constant and equals to the initial temperature of the substrate material in this region. The respective boundary conditions are:

r at infinity $\Rightarrow$ $r = \infty$: $T(\infty, z, t) = T_o$ (specified)

z at infinity $\Rightarrow$ $z = \infty$: $T(r, \infty, t) = T_o$ (specified)

At the symmetry axis, maximum temperature is assumed and the convection boundary condition is considered at the workpiece surface, i.e.:

At symmetry axis $\Rightarrow$ $r = 0$: $\dfrac{\partial T(0, z, t)}{\partial r} = 0$

and

At the surface $\Rightarrow$ $z = 0$: $k \dfrac{\partial T(r, 0, t)}{\partial z} = h\big(T(r, 0, t) - T_o\big)$

where h is taken as 10 $\mathrm{W\,m^{-2}\,K^{-1}}$ due to natural convection from the surface [17].

Since the evaporation temperature depends on the pressure and this relation is not known for steel vapor, it is assumed that the substrate material has single melting and boiling temperatures. Moreover, once the phase change initiates, a mushy zone (mutually existence of two-phases) is introduced across the interface of two phases (Fig. 1). During the phase change process, including the mushy zone, temperature of the substrate material remains the same, but its enthalpy changes in this region. This situation can be formulated via energy balance in the mushy zone. It should be noted that nominal laser pulse length is 24 ns, therefore, the flow in the vapor and liquid layer during the heating process is neglected, i.e., 1 μm of fluid motion, in radial or

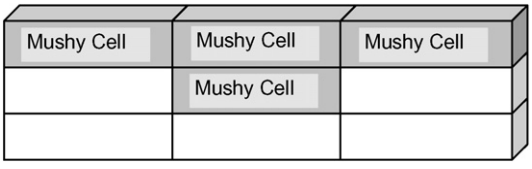

Fig. 1. A schematic view of the mushy zone.

axial direction, in the liquid layer requires the liquid velocity in the order of 1000 m s^{-1}, which may not be the case that occurs in the present simulations; consequently, during the short heating period, the fluid motion in the liquid and vapor layers is assumed not to influence the heat transfer mechanism in these zones. Consider a differential element in the mushy zone (Fig. 1) and let x_m is the mass fraction of liquid present in the element. Energy content (ΔU) of the differential element with volume $\Delta\forall$ at melting temperature T_m can be written as:

$$\Delta U = \rho_m \Delta\forall\big[x_m\big(L_m + c_{p_m}(T_m - T_{\text{ref}})\big) + c_{p_s}(1 - x_m)(T_m - T_{\text{ref}})\big] \tag{3}$$

where

$$x_m = \frac{m_m}{m_m + m_s}$$

$T_{\text{ref}}, x_m, m_m, m_s$ are reference temperature for enthalpy, quality (mass fraction) of liquid, mass of liquid and mass of solid in the element, respectively. After assuming specific heat of melt is the same as the solid at the melting temperature ($c_{p_s} = c_{p_m}$ at $T = T_m$), and differentiation of Eq. (3) with time yields:

$$\frac{\partial u}{\partial t} = \rho_m L_m \frac{\partial x_m}{\partial t}$$
$$\text{since } c_{p_m}(T_m - T_{\text{ref}}) = \text{const} \quad \text{and} \quad u = \frac{U}{\forall}. \tag{4}$$

Substituting Eq. (4) into Eq. (1) and re-arrangement results the energy equation for the differential element in the mushy zone:

$$\rho_m L_m \frac{\partial x_m}{\partial t} = \frac{k_m}{r}\frac{\partial}{\partial r}\left(r\frac{\partial T}{\partial r}\right) + k_m \frac{\partial^2 T}{\partial z^2} + S_o \tag{5}$$

Eq. (5) is valid in the mushy zone where $0 \leqslant x_m \leqslant 1$, i.e. temperature of the cells with $0 \leqslant x_m \leqslant 1$ is set to melting temperature ($T = T_m$). For the situation $x_m = 1$, liquid phase occurs and Eq. (1) is used to determine the temperature rise in the liquid heating with using the liquid thermal properties in the equation. Moreover, the liquid heating continues until the boiling point is reached in the substrate material; in which case, a new mushy zone is formed. In this case, Eq. (5) is modified for a differential element in the mushy zone subjected to evaporation, i.e.:

$$\rho_b L_b \frac{\partial x_b}{\partial t} = \frac{k_b}{r}\frac{\partial}{\partial r}\left(r\frac{\partial T}{\partial r}\right) + k_b \frac{\partial^2 T}{\partial z^2} + S_o \tag{6}$$

Eq. (6) is applicable for temperature $T = T_b$ and $0 \leqslant x_b \leqslant 1$ in the mushy zone (partially liquid partially vapor zone); in which case, temperature of the cells with $0 \leqslant x_b \leqslant 1$ is set to the boiling temperature of the substrate material ($T = T_b$). It should be noted that x_m is replaced with x_b in Eq. (5), which represents the fraction of vapor phase in the differential element. The calculation of x_b is the same as x_m, provided that latent heat of fusion is replaced with latent heat of evaporation of the substrate material in Eq. (5) in the later.

The boundary condition at the evaporating surface is introduced in relation to Eq. (6). In this case, the temperature along the evaporated surface is kept at boiling temperature of the substrate material, i.e., the cells in the evaporated region are kept at boiling temperature, i.e.:

In the mushy zone, at $z = z_b \Rightarrow T(r, z_b, t) = T_b$

where z_b represents the axial location at the evaporated surface.

Eqs. (5) and (6) provide the relative position of solid–liquid and liquid–vapor interface in the substrate material. Liquid–vapor interface determines the shape and size of the cavity generated during evaporation process.

3. Transiently developing vapor jet

The vapour front emerging from the laser induced cavity is modelled numerically using a control volume approach and the fluid dynamic/mass transfer model is accommodated in the analysis. The laser produced cavity shape and its temporal progression are employed in the simulations. In this case, the time-varying cavity shape, mass flux of the vapour and the temperature distribution at the cavity surface are the inputs for the simulations. In the flow analysis, the time averaged conservation equations are accommodated for an unsteady, incompressible, axisymmetric turbulent flow situation resembling the vapor jet expansion. The Standard k–ε turbulence model is used to account for the turbulence. Moreover, the species transport model is also used to account for the mass transfer of the vapor jet from the cavity into the stagnant water ambient. It should be noted that all the unknown quantities are time-averaged since the RANS equations are used.

Continuity equation:

$$\frac{1}{r}\frac{\partial(rV_r)}{\partial r} + \frac{\partial V_z}{\partial r} = 0 \tag{7}$$

Radial momentum:

$$\frac{\partial(\rho V_r)}{\partial t} + \frac{1}{r}\frac{\partial(\rho r V_r^2)}{\partial r} + \frac{\partial(\rho V_r V_z)}{\partial z} = -\frac{\partial p}{\partial r} + \frac{2}{r}\frac{\partial}{\partial r}\left(\mu_{\text{eff}} r\frac{\partial V_r}{\partial r}\right) + \frac{\partial}{\partial z}\left(\mu_{\text{eff}}\frac{\partial V_r}{\partial z}\right) + \frac{\partial}{\partial z}\left(\mu_{\text{eff}}\frac{\partial V_z}{\partial z}\right) - 2\mu_{\text{eff}}\frac{V_r}{r^2} \tag{8}$$

Axial momentum:

$$\frac{\partial(\rho V_z)}{\partial t} + \frac{1}{r}\frac{\partial(\rho r V_r V_z)}{\partial r} + \frac{\partial(\rho V_z^2)}{\partial z} = -\frac{\partial p}{\partial z} + \frac{1}{r}\frac{\partial}{\partial r}\left(\mu_{\text{eff}} r\frac{\partial V_z}{\partial r}\right) + 2\frac{\partial}{\partial z}\left(\mu_{\text{eff}}\frac{\partial V_z}{\partial z}\right) + \frac{1}{r}\frac{\partial}{\partial r}\left(\mu_{\text{eff}} r\frac{\partial V_r}{\partial z}\right) \tag{9}$$

where

$$\mu_{\text{eff}} = \mu + \mu_t\colon\ \mu_t = \frac{\rho C_\mu K^2}{\varepsilon}\colon\ C_\mu = 0.09$$

Energy equation:

$$\frac{\partial(\rho E)}{\partial t}+\frac{1}{r}\frac{\partial(rV_r\rho E)}{\partial r}+\frac{\partial(V_z\rho E)}{\partial z}$$
$$=\frac{1}{r}\frac{\partial}{\partial r}\left(rk_{\text{eff}}\frac{\partial T}{\partial r}\right)+\frac{\partial}{\partial z}\left(k_{\text{eff}}\frac{\partial T}{\partial z}\right)$$
$$+\left[\frac{1}{r}\frac{\partial}{\partial r}\left(rh_{\text{vapor}}\left(\rho D+\frac{\mu_t}{Sc_t}\right)\frac{\partial Y_{\text{vapor}}}{\partial r}\right)\right.$$
$$\left.+\frac{\partial}{\partial z}\left(h_{\text{vapor}}\left(\rho D+\frac{\mu_t}{Sc_t}\right)\frac{\partial Y_{\text{vapor}}}{\partial z}\right)\right]$$
$$+\left[\frac{1}{r}\frac{\partial}{\partial r}\left(rh_{\text{water}}\left(\rho D+\frac{\mu_t}{Sc_t}\right)\frac{\partial Y_{\text{water}}}{\partial r}\right)\right.$$
$$\left.+\frac{\partial}{\partial z}\left(h_{\text{water}}\left(\rho D+\frac{\mu_t}{Sc_t}\right)\frac{\partial Y_{\text{water}}}{\partial z}\right)\right] \quad (10)$$

where $E=Y_{\text{water}}h_{\text{water}}+Y_{\text{vapor}}h_{\text{vapor}}$, after neglecting the contribution of kinetic energy. Enthalpy of vapor and water are:

$$h_{\text{vapor}}=\int_{T_{\text{ref}}}^{T}Cp_{\text{vapor}}\,\mathrm{d}T=Cp_{\text{vapor}}(T-T_{\text{ref}}) \quad (11)$$

$$h_{\text{water}}=\int_{T_{\text{ref}}}^{T}Cp_{\text{water}}\,\mathrm{d}T=Cp_{\text{water}}(T-T_{\text{ref}}) \quad (12)$$

In Eqs. (7)–(9), the properties and parameters are:

$k_{\text{eff}}=k+k_t$: $k_t=Cp\dfrac{\mu_t}{Pr_t}$ and $D=2.88\times10^{-5}$ [$\text{m}^2\,\text{s}^{-1}$]:

$Sc_t=0.7$: $Pr_t=0.85$: $T_{\text{ref}}=298.15$ K

Turbulence kinetic energy equation, K:

$$\frac{\partial(\rho K)}{\partial t}+\frac{1}{r}\frac{\partial(\rho rV_rK)}{\partial r}+\frac{\partial(\rho V_zK)}{\partial z}$$
$$=\frac{1}{r}\frac{\partial}{\partial r}\left(\frac{\mu_{\text{eff}}}{\sigma_K}r\frac{\partial K}{\partial r}\right)+\frac{\partial}{\partial z}\left(\frac{\mu_{\text{eff}}}{\sigma_K}\frac{\partial K}{\partial z}\right)-\rho\varepsilon+P_K \quad (13)$$

where

$$P_K=\mu_{\text{eff}}\left[2\left\{\left(\frac{\partial V_z}{\partial r}\right)^2+\left(\frac{\partial V_r}{\partial r}\right)^2+\left(\frac{V_r}{r}\right)^2\right\}\right.$$
$$\left.+\left(\frac{\partial V_z}{\partial r}+\frac{\partial V_r}{\partial z}\right)^2\right]$$

Rate of dissipation equation, ε:

$$\frac{\partial(\rho\varepsilon)}{\partial t}+\frac{1}{r}\frac{\partial(\rho rV_r\varepsilon)}{\partial r}+\frac{\partial(\rho V_z\varepsilon)}{\partial z}$$
$$=\frac{1}{r}\frac{\partial}{\partial r}\left(\frac{\mu_{\text{eff}}}{\sigma_\varepsilon}r\frac{\partial\varepsilon}{\partial r}\right)$$
$$+\frac{\partial}{\partial z}\left(\frac{\mu_{\text{eff}}}{\sigma_\varepsilon}\frac{\partial\varepsilon}{\partial z}\right)-C_1\frac{\varepsilon}{K}P_K-C_2\rho\frac{\varepsilon^2}{K} \quad (14)$$

where

$$P_K=\mu_{\text{eff}}\left[2\left\{\left(\frac{\partial V_z}{\partial r}\right)^2+\left(\frac{\partial V_r}{\partial r}\right)^2+\left(\frac{V_r}{r}\right)^2\right\}\right.$$
$$\left.+\left(\frac{\partial V_z}{\partial r}+\frac{\partial V_r}{\partial z}\right)^2\right]$$

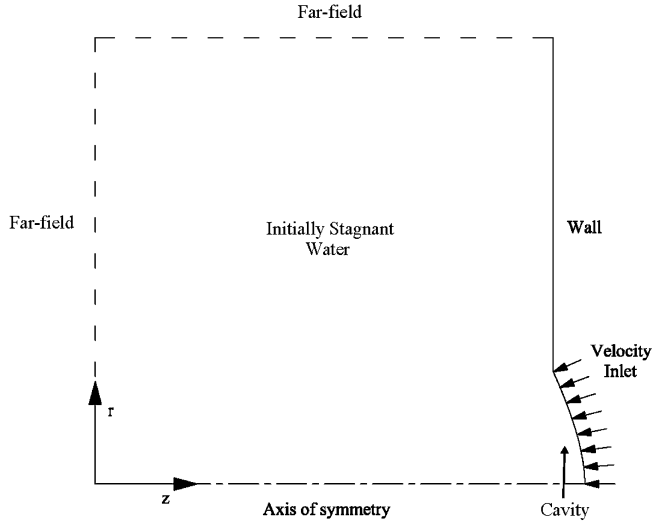

Fig. 2. Solution domain of an axisymmetric jet expansion emanating from cavity.

and

$$\sigma_K=1,\qquad \sigma_\varepsilon=1.3,\qquad C_1=1.44,\qquad C_2=1.92$$

Species transport equation:

$$\frac{\partial(\rho Y_{\text{vapor}})}{\partial t}+\frac{1}{r}\frac{\partial(rV_r\rho Y_{\text{vapor}})}{\partial r}+\frac{\partial(V_z\rho Y_{\text{vapor}})}{\partial z}$$
$$=\left[\frac{1}{r}\frac{\partial}{\partial r}\left(r\left(\rho D+\frac{\mu_t}{Sc_t}\right)\frac{\partial Y_{\text{vapor}}}{\partial r}\right)\right.$$
$$\left.+\frac{\partial}{\partial z}\left(\left(\rho D+\frac{\mu_t}{Sc_t}\right)\frac{\partial Y_{\text{vapor}}}{\partial z}\right)\right] \quad (15)$$

where $Y_{\text{water}}=1-Y_{\text{vapor}}$.

Initial and boundary conditions: Fig. 2 shows the solution domain.

Symmetry axis: $(r=0)$

At the symmetry axis all the unknown quantities are considered to be maximum accept the r-direction velocity, which is zero.

$$\left.\frac{\partial V_z}{\partial r}\right|_{\substack{z=z\\r=0}}=0:\ V_r(z,0)=0:\ \left.\frac{\partial T}{\partial r}\right|_{\substack{z=z\\r=0}}=0:\ \left.\frac{\partial K}{\partial r}\right|_{\substack{z=z\\r=0}}=0:$$
$$\left.\frac{\partial\varepsilon}{\partial r}\right|_{\substack{z=z\\r=0}}=0:\ \left.\frac{\partial Y_{\text{vapor}}}{\partial r}\right|_{\substack{z=z\\r=0}}=0$$

Outflow: (At $z=0$)

At the outflow boundary perpendicular to the z-axis the normal derivatives of all the unknown quantities are considered to be zero accept the r-direction velocity, whose value is zero as required from the continuity equation.

$$\left.\frac{\partial V_z}{\partial z}\right|_{\substack{z=0\\r=r}}=0:\ V_r(0,r)=0:\ \left.\frac{\partial T}{\partial z}\right|_{\substack{z=0\\r=r}}=0:\ \left.\frac{\partial K}{\partial r}\right|_{\substack{z=0\\r=r}}=0$$
$$\left.\frac{\partial\varepsilon}{\partial r}\right|_{\substack{z=0\\r=r}}=0:\ \left.\frac{\partial Y_{\text{vapor}}}{\partial r}\right|_{\substack{z=0\\r=r}}=0$$

Outflow: (At $r=r_{\max}$)

At the outflow boundary perpendicular to the r-axis the normal derivatives of all the unknown quantities are considered to

be zero accept the z-direction velocity, whose value is zero as required from the continuity equation.

$$V_z(z, r_{\max}) = 0:\ \left.\frac{\partial V_r}{\partial r}\right|_{\substack{z=z\\ r=r_{\max}}} = 0:\ \left.\frac{\partial T}{\partial r}\right|_{\substack{z=z\\ r=r_{\max}}} = 0:$$

$$\left.\frac{\partial K}{\partial r}\right|_{\substack{z=z\\ r=r_{\max}}} = 0$$

$$\left.\frac{\partial \varepsilon}{\partial r}\right|_{\substack{z=z\\ r=r_{\max}}} = 0:\ \left.\frac{\partial Y_{\text{vapor}}}{\partial r}\right|_{\substack{z=0\\ r=r_{\max}}} = 0$$

Solid wall: $z = f(r,t)$

The surface of the substrate material including the cavity surface acts like a solid wall in the solution domain and hence a no-slip and no-temperature jump boundary conditions are considered. At the cavity surface, the vapor mass fraction is considered to be one whereas the water mass fraction is considered to be zero. In this case, the function $f(r,t)$ defining the cavity wall shape, as obtained from the heat transfer analysis, can be presented in algebraic form. It should be noted that the temporal development of the cavity in axial and radial directions is computed using Eqs. (1)–(6). Once the cavity profile in axial and radial directions is obtained for each time step, an algebraic equation is introduced, using the polynomial fitting technique, to resemble the temporal behavior of the cavity shape through using the computed data available for time steps. Moreover, the algebraic equation resembling the cavity shape is in the functional form such that time (t) and radial location (r) are set as independent variables for fixed axial (Δz) and radial space (Δr) increments. Consequently, for each heating time step and defined radial locations, cavity shape can be obtained from the functional relation. This arrangement is necessary due to in the solution of flow Eqs. (7)–(15), solid wall at the cavity surface should be defined. In addition, this functional arrangement of the temporal behavior of cavity surface enables to solve flow equations. The vapor mass generated due to recession of the cavity surface varies in time as well as in space coordinates. The vapor mass flow generated during cavity surface recession is the source of the mass of the vapor jet emanating from the cavity surface.

Equation resembling the temporally recessing cavity surface is:

$$f(r,t) = \left[c\left((r/\Delta r)^2 - r_{\max}^2\right) + d\left((r/\Delta r)^3 - r_{\max}^3\right)\right](\rho_l/\rho_v)\Delta z$$

where

$$c = cc_3 + cc_2(t/\Delta t) + cc_1(t/\Delta t)^2$$

$$cc_1 = 4.4499 \times 10^{-6}:\ cc_2 = -0.0026726:\ cc_3 = -0.15077$$

and

$$d = cd_3 + cd_2(t/\Delta t) + cd_1(t/\Delta t)^2$$

$$cd_1 = -1.7974 \times 10^{-7}:\ cd_2 = 0.00011187:\ cd_3 = 0.0062477$$

and

$$r_{\max} = cr_5 + cr_4(t/\Delta t) + cr_3(t/\Delta t)^2 + cr_2(t/\Delta t)^3 + cr_1(t/\Delta t)^4$$

where

$$cr_1 = -2.5982 \times 10^{-9}:\ cr_2 = 2.0455 \times 10^{-6}:$$

$$cr_3 = -0.00059955:\ cr_4 = 0.086871:\ cr_5 = 7.7763$$

The numerical values for the space increments are:

$$\Delta z = 3.2415 \times 10^{-8}\ \text{m}$$

$$\Delta r = 8.3333 \times 10^{-8}\ \text{m}$$

The recession velocity of the cavity wall as obtained from the above analysis can be represented in the algebraic form. In this case, the cavity size is limited with $0 \leqslant r \leqslant r_{\max}$. Therefore, the recession velocity of the cavity along the vertical direction is:

$$V_z\big(f(r,t), r\big) = \frac{\rho_l}{\rho_v}\frac{\partial f}{\partial t}\frac{\partial f/\partial r}{\sqrt{1 + (\partial f/\partial r)^2}} \quad \text{for } 0 \leqslant r \leqslant r_{\max}$$

Moreover, out side of the cavity a stationary solid wall is considered (Fig. 2). The recession velocity along the vertical axis is, therefore:

$$V_z\big(f(r,t), r\big) = 0 \quad \text{for } r > r_{\max}$$

The recession velocity of the cavity along the radial direction is:

$$V_r\big(f(r,t), r\big) = -\frac{\rho_l}{\rho_v}\frac{\partial f}{\partial t}\frac{1}{\sqrt{1 + (\partial f/\partial r)^2}} \quad \text{for } 0 \leqslant r \leqslant r_{\max}$$

Out side of the cavity a stationary solid wall is considered (Fig. 2). The recession velocity along the radial direction is, therefore:

$$V_r\big(f(r,t), r\big) = 0 \quad \text{for } r > r_{\max}$$

Temperature at the cavity wall is determined from the heat transfer analysis and can be presented in algebraic form. In this case, temperature at the cavity wall is the same as the boiling temperature of the substrate material (T_b), i.e.:

$$T\big(f(r,t), r\big) = T_b \quad \text{for } 0 \leqslant r \leqslant r_{\max}$$

$$T\big(f(r,t), r\big) = 2834\exp\left(-btemp\left((r/\Delta r) - r_{\max}\right)^2\right) + 300 \quad \text{for } r > r_{\max}$$

where

$$btemp = ctemp(t/\Delta t)^2 + dtemp(t/\Delta t) + etemp:$$

$$ctemp = 1.0370442955011 \times 10^{-6}:$$

$$dtemp = -3.39682806506743 \times 10^{-5}:$$

$$etemp = 0.0241815719639816$$

Turbulence kinetic energy and dissipation of the jet in the cavity wall region is assumed to be constant and taken as:

$$K\big(f(r,t), r\big) = 1\ (\text{m s}^{-1})^2 \quad \text{and} \quad \varepsilon\big(f(r,t), r\big) = 1\ (\text{m s}^{-1})^2$$

$$Y_{\text{vapour}}\big(f(r,t), r\big) = 1 \quad \text{for } 0 \leqslant r \leqslant r_{\max}$$

$$Y_{\text{vapour}}\big(f(r,t), r\big) = 0 \quad \text{for } r > r_{\max}$$

Initial conditions:

Initially the ambient water is assumed as stagnant; therefore, the z and r-directions velocity components are zero. Initially, temperature is considered to be uniform and equal to 300 K in water ambient and the vapor mass fraction is zero whereas the water mass fraction is one throughout the domain.

$$V_z(z,r)=0;\ V_r(z,r)=0;\ T(z,r)=300\ \text{K};\ K(z,r)=1$$
$$\varepsilon(z,r)=1;\ Y_{\text{vapour}}(z,r)=0$$

4. Numerical solution

4.1. Phase change process

Eq. (1) is applicable to solid and liquid heating, Eq. (5) is applicable to mushy zone at solid–liquid interface and Eq. (6) is applicable to mushy zone at liquid–vapor interface. To discretize the governing equations, a finite difference scheme is introduced. The details of the numerical scheme are given in [18]. To compute the equations discretized for temperature field and relative positions of solid–liquid and liquid–vapor interface, an implicit scheme is used, i.e., using the initial conditions, the temperature in the whole domain is calculated for following time steps with the respective conditions.

The calculation domain is divided into grids and grid independence test is performed for different grid size and orientation and the grid size resulting grid independent solution is used, which is 100 × 120 mesh points in the r- and z-axes (Fig. 3). A computer program based on implicit scheme is developed to compute the temperature field.

The material properties and pulse intensity used in the simulations are given in Tables 1 and 2, respectively. It should be noted that the laser pulse properties employed in the simulations resemble the actual pulse used in the experiment (Fig. 4).

4.2. Transiently developing vapor jet (front)

A control volume approach is employed when discretizing the governing equations [19]. A staggered grid arrangement is used in which the velocities are stored at a location midway between the grid points, i.e., on the control volume faces. All other variables including pressure are calculated at the grid points. This arrangement gives a convenient way of handling the pressure linkages through the continuity equation and is known as Semi-Implicit Method for Pressure-Linked Equations (SIMPLE) algorithm. The details of this algorithm are given in [19].

The computer program used for the present simulation can handle a non-uniform grid spacing. Along the radial direction fine uniform grid spacing is allocated at the inlet (in cavity symmetry axis region) while gradually increasing spacing is considered away from the inlet (in the cavity edge region). Along the axial direction, again fine uniform grid spacing is used inside and near the cavity while the grid spacing gradually increases away from the cavity. The number of grid points in the radial direction is 300 while 215 grid points are used in the axial direction. Since the problem is involved with the moving boundary, the moving meshes are accommodated in the cavity to account

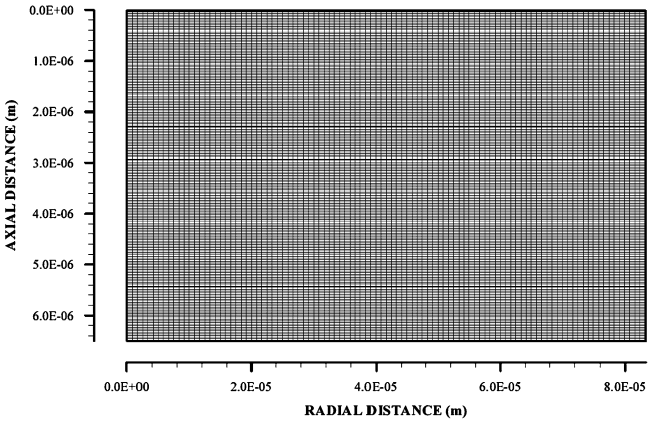

Fig. 3. A layout of grid used in the simulations of phase change heat transfer.

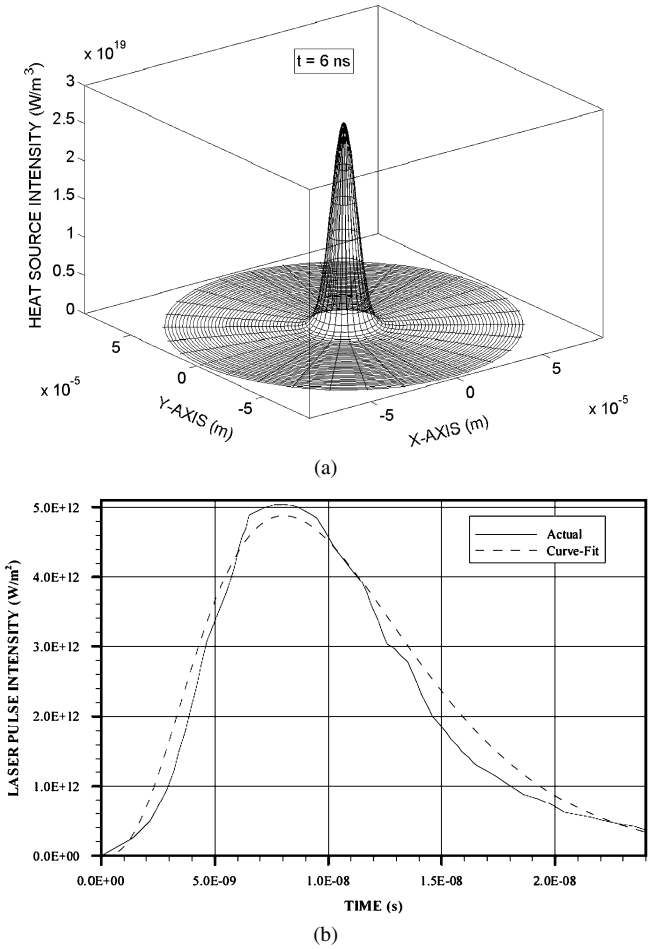

Fig. 4. Laser pulse intensity used in the simulations. (a) Spatial distribution of laser pulse. (b) Temporal variation of laser pulse.

for the cavity recession with time. The actual computational grid is shown in Fig. 5. The grid independence test is conducted and grid size (215 × 300) resulting in grid independent solution is used in the simulations.

Eight variables are computed at all grid points. These are the two velocity components, local pressure, two turbulence quantities, temperature and two mass fractions. The properties of substrate material used in the simulations are given in Table 3.

Table 1
Thermal properties of steel used in the simulations

T_m [K]	T_b [K]	ρ [kg m^{-3}]	Cp [J kg^{-1} K^{-1}]	k W m^{-1} K^{-1}]	δ [1 m^{-1}]	L_m [J kg^{-1}]	L_b [J kg^{-1}]
1810	3134	7860	420	63	6.17×10^6	247 112	6 213 627

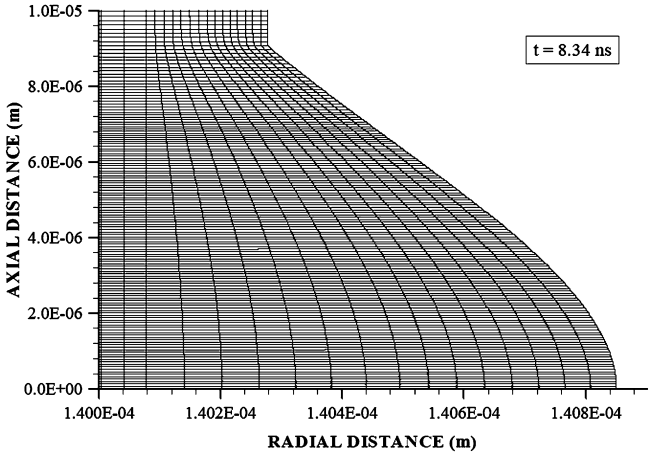

Fig. 5. Moving mesh used in the simulations. Mesh points in the cavity are shown at 8.34 ns of the heating time.

Table 2
Laser pulse intensity used in the simulations

Peak intensity [W m^{-2}]	Gaussian parameter [1 m^{-1}]	Nominal pulse length [ns]
9×10^{12}	120 000	24

Table 3
Properties of water and vapor front used in the simulations

	Water	Vapor front
Density [kg m^{-3}]	998.2	50, 800
Viscosity [kg m^{-1} s^{-1}]	0.001003	1.34×10^{-5}
Mass diffusivity [m^2 s^{-1}]	2.88×10^{-5}	
Specific heat capacity [J kg^{-1} K^{-1}]	4182	2014
Thermal conductivity [W m^{-1} K^{-1}]	0.6	0.0261
Molecular weight [kg kg^{-1}mol^{-1}]	18.0152	56

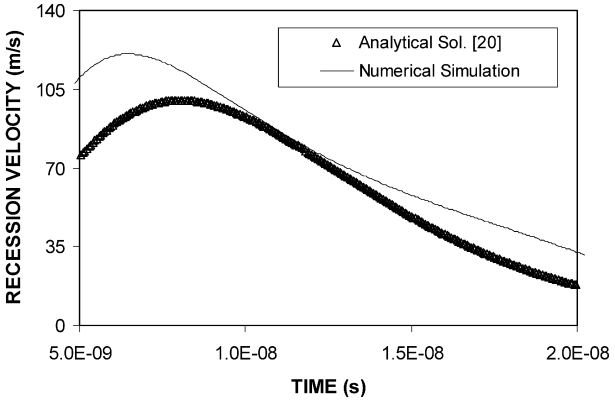

Fig. 6. Comparison of recession velocity obtained from present predictions along the symmetry axis and one-dimensional analytical solution [20].

5. Results and discussions

Laser heating of surfaces is considered and phase change processes during the heating pulse are modeled. The recession velocity of the surface and mushy zones at solid–liquid and liquid–vapor phases are predicted. Vapor front expansion into stagnant water ambient is also modeled and flow field as well as jet penetration into water are predicted. Since the vapor density of the vapor jet is not known, vapor density of 800 kg m^{-3} and 50 kg m^{-3} are assumed in the analysis. The predictions of flow properties due to two vapor densities are compared. Moreover, to validate the predictions, analytical solution obtained from the previous study [20] is used to compute the recession velocity.

Fig. 6 shows the recession velocity of the evaporating surface predicted from the present study and the one-dimensional analytical solution [20]. The recession velocity predicted agrees with the one-dimensional closed form solutions, provided that some small discrepancies occur between both results. This can be explained in terms of the affects of the radial heat conduction and spatial distribution of the laser beam intensity, which are accommodated in the present model while omitted in the one-dimensional analysis [20].

Fig. 7 shows temperature contours in the region of irradiated spot for four heating periods. The cavity wall lies on the contour of evaporation temperature. Evaporation of the surface initiates after 1.35 ns of the initiation of the laser pulse. Once the evaporation starts, the depth of evaporated region extends towards the axial direction and radial extension is mainly associated with the laser intensity distribution in the radial direction, which is Gaussian. Extension of contours of vapor temperature along the symmetry axis is more than its counterpart along the axial direction at any other radial locations. This is because of the absorption of laser beam. In this case, at the symmetry axis, laser beam intensity is high and energy distribution in the absorption depth along the symmetry axis enables more energy being absorbed by the substrate material than any other radial location. This in turn, enhances the evaporation rate and increases the depth of evaporated region along the symmetry axis. This situation is more pronounced with increasing heating period.

Fig. 8 shows 3-dimensional view of cavity shape and the cavity cross-section. It is observed that near conical cavity shape is resulted after the initiation of evaporation. In addition, the mushy zone formation at interfaces of solid–liquid and liquid–vapor is evident. The size of mushy zone is small particularly at interface of solid–liquid phases. This is because of the latent heat of fusion, which is considerably smaller than that of vapor. Moreover, the size of the mushy zone is small in the region close to the cavity edges. This is because of the laser incident energy, which is less in this region due to Gaussian distribution of laser beam intensity. In addition, temperature

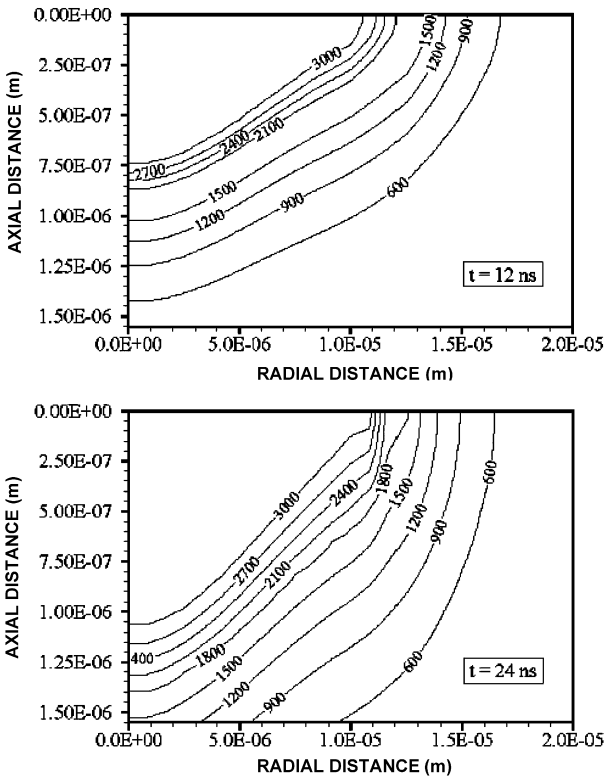

Fig. 7. Temperature contours at two different heating periods.

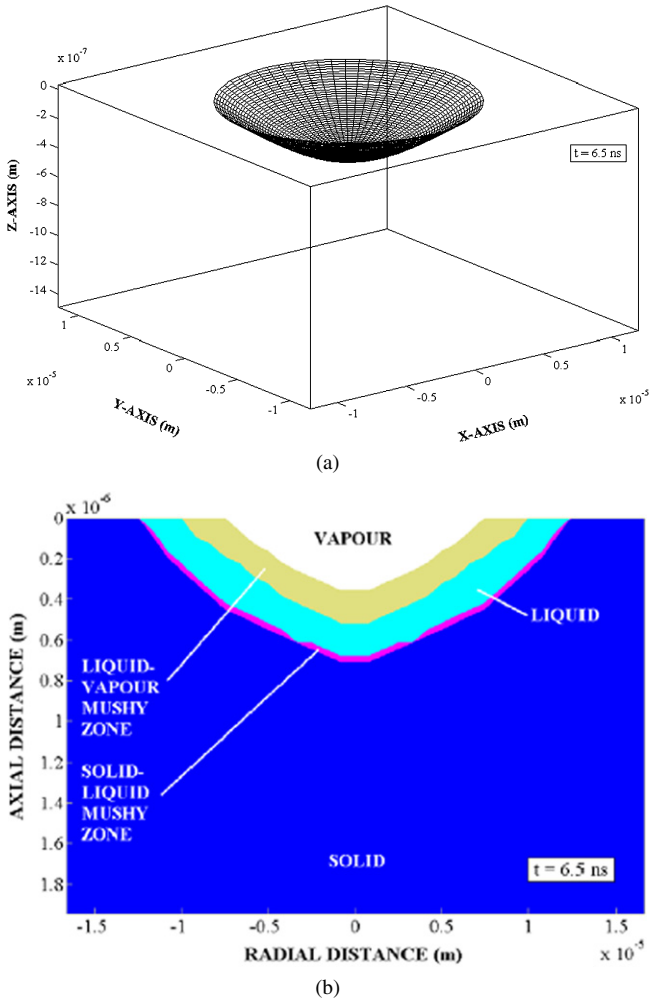

Fig. 8. Three-dimensional view of laser produced cavity and cavity cross section. (a) Three-dimensional view of laser produced cavity. (b) Cavity cross-section.

gradient in the axial direction in this region is smaller than that of symmetry axis, i.e., heat flow in the axial direction at the cavity centre is larger than that corresponding to in the region of cavity edges.

Figs. 9(a) and (b) show velocity contours in and around the cavity for two vapor densities. The size of the domain presented in Figs. 9(a) and (b) is larger than the cavity size. This is due to that the vapor jet emanating from the cavity expands into cavity as well as into the cavity surrounding, which is water ambient, during the time domains considered. In this case, the size of the jet expansion is much larger than the cavity size. In the case of vapor density 800 kg m^{-3}, temporal extension of cavity in the radial direction results in complex flow structure in the region of the cavity edge. Moreover, jet expansion along the symmetry axis is high in the early heating period. As the heating period increases, jet expansion in the radial direction also increases. This is because of the relatively low density jet expansion into high density stagnant water. In the early heating period, jet emanating from cavity purges the stagnant water in the axial direction more than in the radial direction. Due to the momentum change during this process, pressure builds up in the frontal region of the jet. In this case, radial expansion of the jet becomes unavoidable due to blockage affect of the pressure build up in the frontal area of the jet in the axial direction. This situation slightly differs for vapor density of 50 kg m^{-3}. In the case of Fig. 9(b), the radial expansion of the jet is evident in the early heating period. It is observed that next to the jet boundary particularly in the region of cavity edge, circulation cell is generated. Moreover, the detachment of the jet after emanating from the cavity is also observed. This is more pronounced during the late heating period ($t \geqslant 7.74$ ns). This indicates that the initial acceleration of the jet is high and once the pressure increases in the frontal area of the jet, radial expansion of the jet becomes more than its axial component. However, continuous vapor mass addition to the jet in the axial direction in the cavity, due to cavity recession, pushes the jet front penetrating into the surrounding fluid. This forms like a jet neck immediately above the cavity exit. Due to the rate of fluid strain, which is high in this region, forms a circulation cell in the vicinity of the jet neck. This appears as a detachment of jet front from the mainstream jet flow. This situation is also seen from Fig. 10, in which pressure variation along the symmetry axis is shown. The peak pressure occurs in the jet above the cavity exit and the locus of the peak pressure moves along the axial direction as the time progresses. Moreover, as the time progresses, the magnitude of pressure reduces.

Fig. 11 shows pressure contours in and around the cavity for four heating periods. The size of the domain presented in Figs. 11(a) and (b) is larger than the cavity size. This is due to that the vapor jet emanating from the cavity expands into cavity as well as into the cavity surrounding, which is water ambient, during the time domains considered. In this case, the size of the

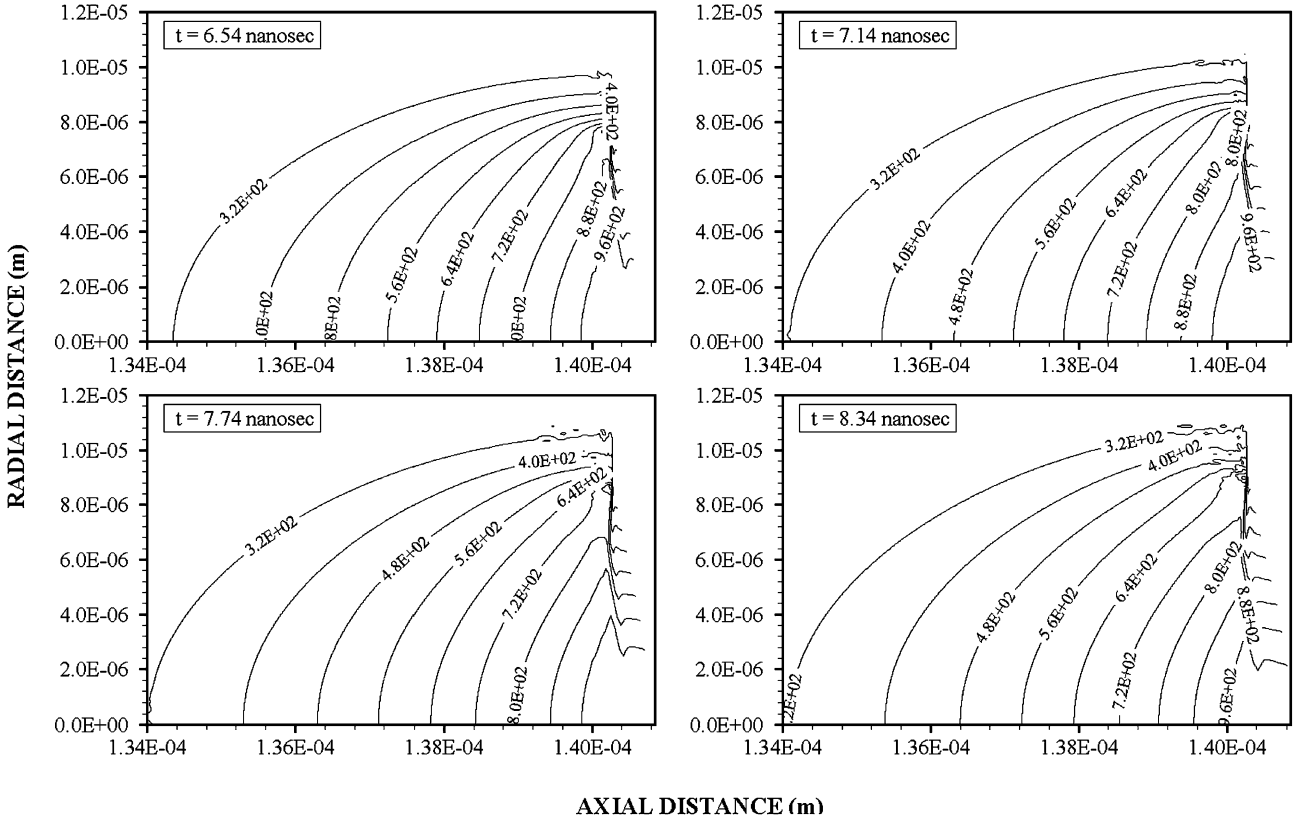

(a)

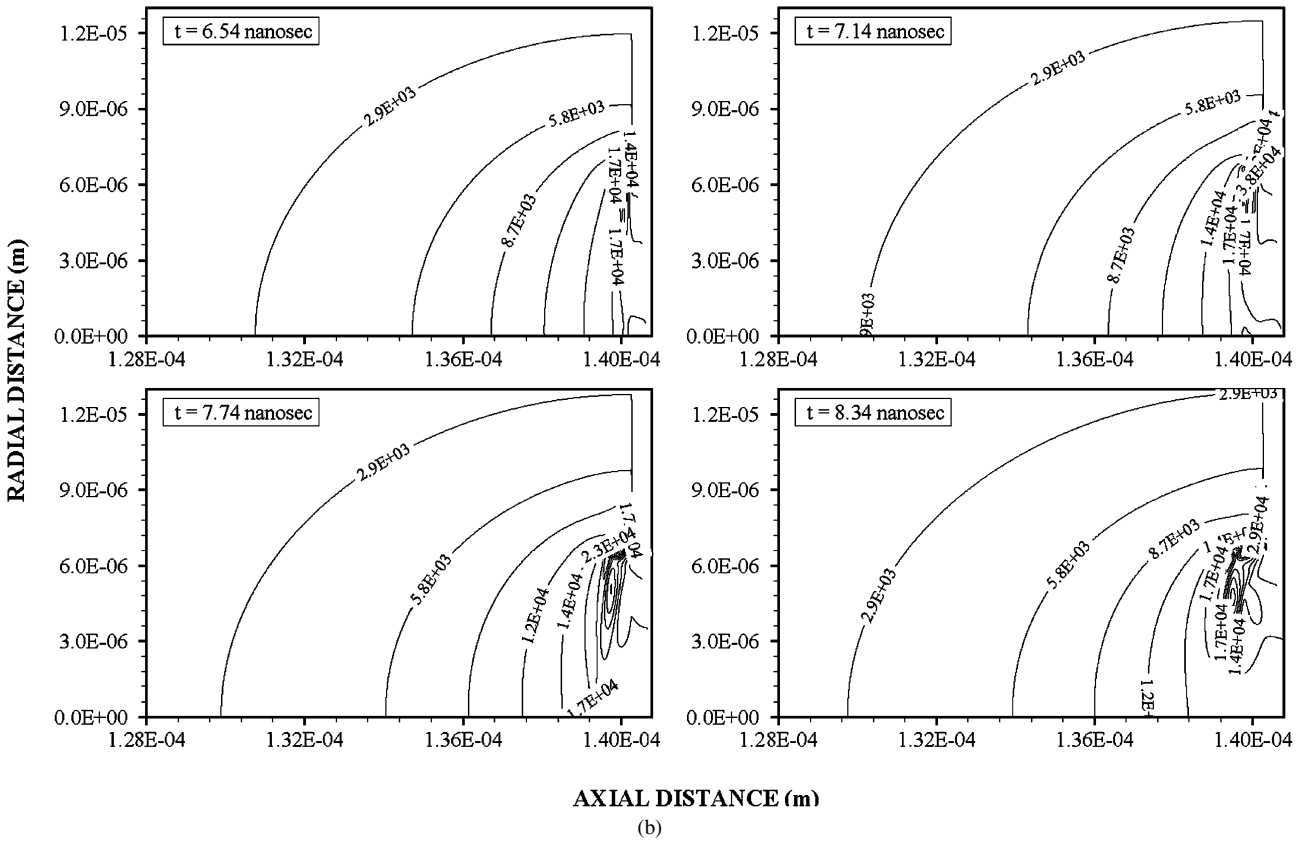

(b)

Fig. 9. (a) Velocity contours for vapor front density of 800 kg m^{-3}. (b) Velocity contours for vapor front density of 50 kg m^{-3}.

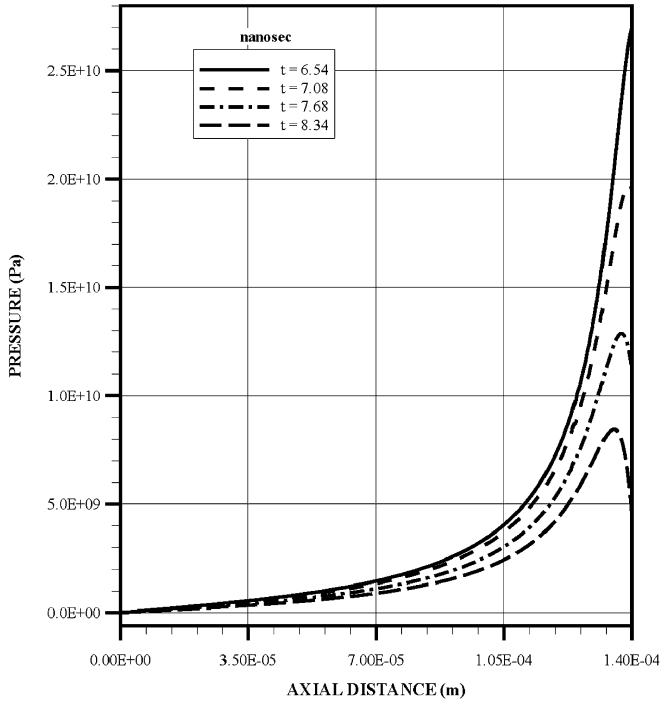

(a)

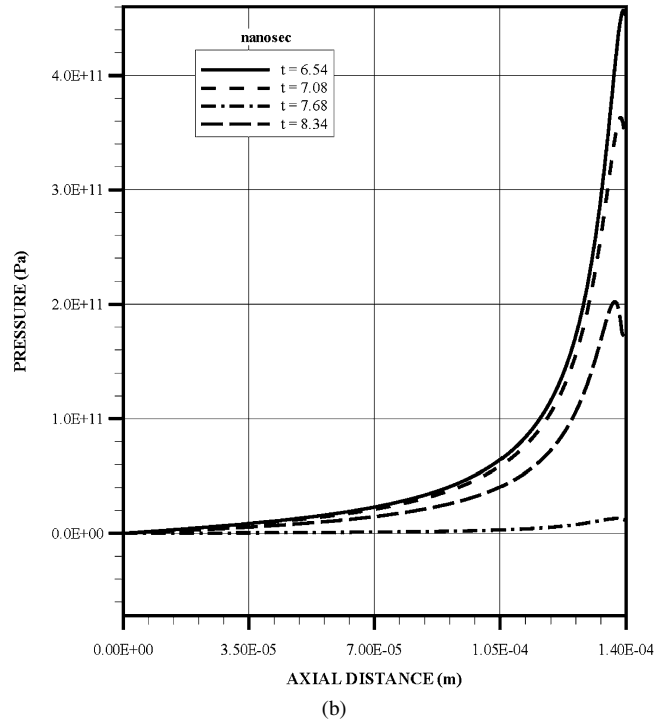

(b)

Fig. 10. Pressure variation along symmetry axis. (a) Vapor front density 800 kg m^{-3}. (b) Vapor front density 50 kg m^{-3}.

jet expansion is much larger than the cavity size. Considerably high pressures are attained particularly in the cavity region due to high expansion velocity of the vapor front. The center of high pressure is resulted in the region close to the cavity edge. This is because of the low recession velocity of the solid surface as well as complex flow structure being developed in this region. High recession velocity of the solid along the symmetry axis lowers the pressure developed in the central region of the cavity.

Fig. 12 shows maximum pressure along the symmetry axis for two vapor front velocities. In the early heating period, the magnitude of maximum pressure is high and as the time progresses it reduces. The attainment of high pressure in the early heating period can be attributed to the recession velocity of the solid surface, which is high in the early heating period. In this case, solid surface recesses towards the solid bulk of the substrate material while vapor front expands opposite to the motion of the recessing solid surface. This in turn results in significant momentum exchange at the interface of vapor–liquid interfaces. Consequently, excessive pressure rise is generated at the interface, which is high in the early heating period.

Fig. 13 shows the location of maximum pressure with time for two vapor front densities. The location of maximum pressure moves towards the cavity exit as the time progresses. This occurs because of the continuous jet production through recession of the melt surface (cavity wall recession). In addition, the cavity recesses opposite to the motion of the jet and the depth of cavity increases by time. In the case of low density, the location moves at early heating times in the cavity due to momentum change with the surrounding fluid. It should be noted that the velocity of the jet emerging from the cavity wall is higher for low density fluid (50 kg m^{-3}) than that of high density fluid (800 kg m^{-3}). Moreover, as time progresses further ($t \geqslant 7.74$ ns) change in the location of maximum pressure becomes small for low density fluid case.

Fig. 14 shows dimensionless penetration depth (Z_t/D) for two vapor front densities. Since the liquid surface recesses, the cavity diameter extends with progressing time. Consequently the magnitude of Z_t/D is influenced by the progression of cavity diameter. Moreover, temporal expansion of cavity diameter is the same for both densities. The magnitude of Z_t/D attains high values in the early heating period and as the time progresses it decays gradually. This may be because of the expansion of cavity diameter and jet penetration in the early durations. However, when comparing Z_t/D corresponding to two densities, both density fluids result in similar penetration depth. Moreover, as the time progresses further, jet penetration into its surroundings makes a local peak. This is due to the complex flow structure generated; in which case, jet momentum along the symmetry axis remains high resulting in high magnitude of jet penetration into stagnant fluid ambient at this particular time.

6. Conclusions

Laser heating of solid surface and phase change processes are considered. The cavity shape and mushy zones at solid–liquid and liquid–vapor interfaces are predicted. Jet emanating from the evaporating surface and expanding into stagnant water is modeled. The jet flow characteristics are predicted for two vapor densities. This is due to that the metal vapor density onset of evaporation is not known, two vapor densities (800 kg m^{-3} and 50 kg m^{-3}) are considered. It is found that the cavity extension along the symmetry axis is larger than that corresponding to the cavity edge. This is due to absorption of laser power intensity, which is high along the symmetry axis. The size of the

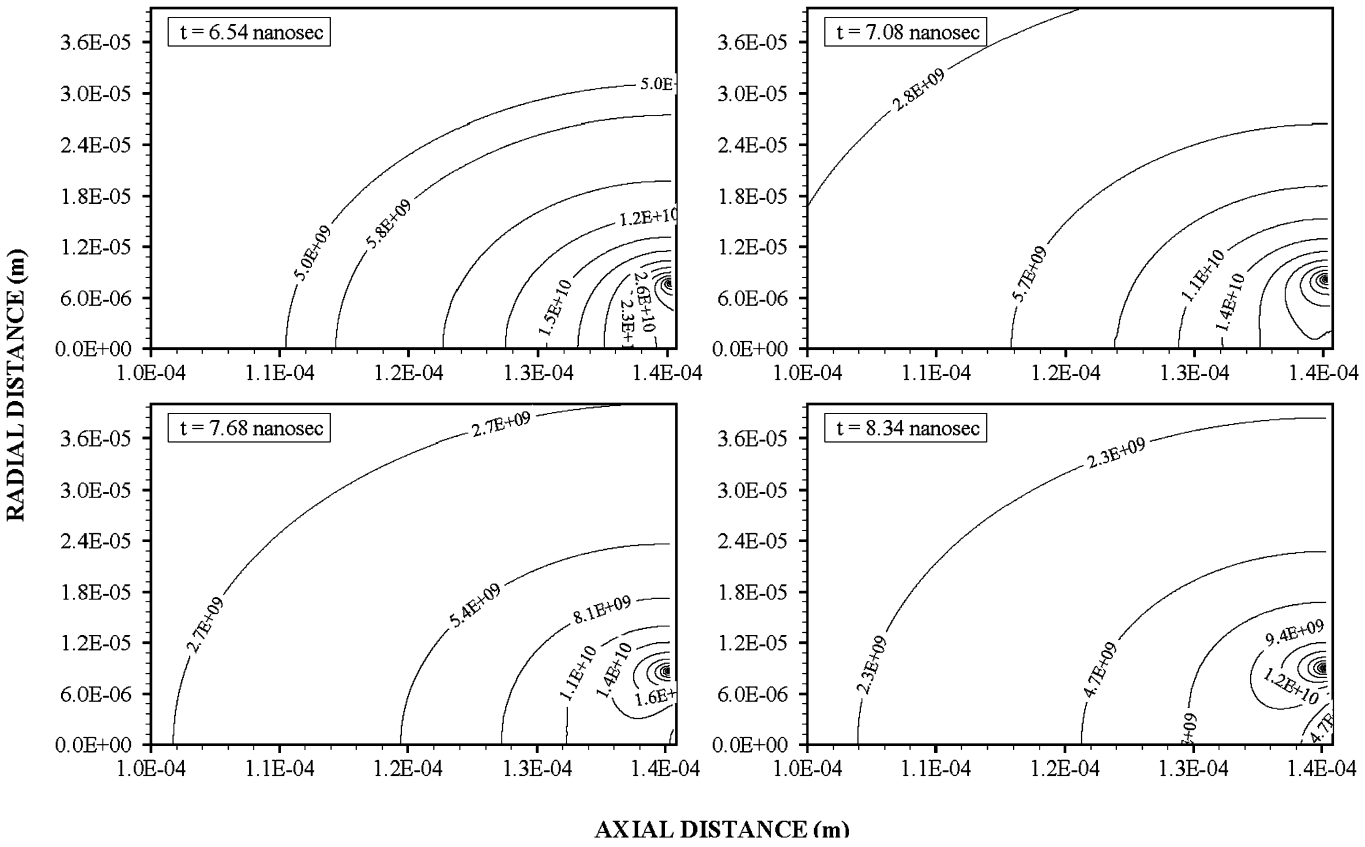

(a)

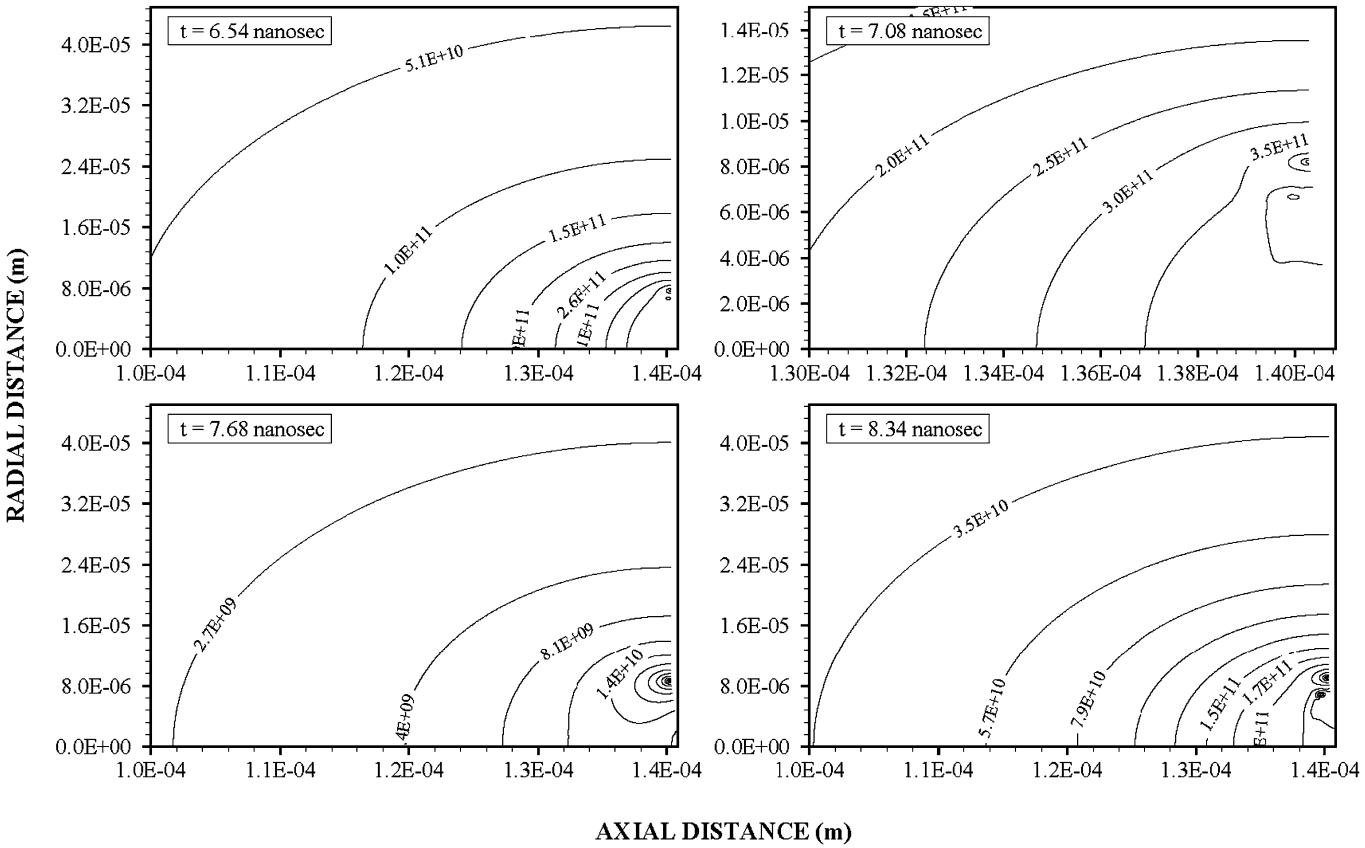

(b)

Fig. 11. (a) Pressure contours for vapor density of 800 kg m^{-3}. (b) Pressure contours for vapor density of 50 kg m^{-3}.

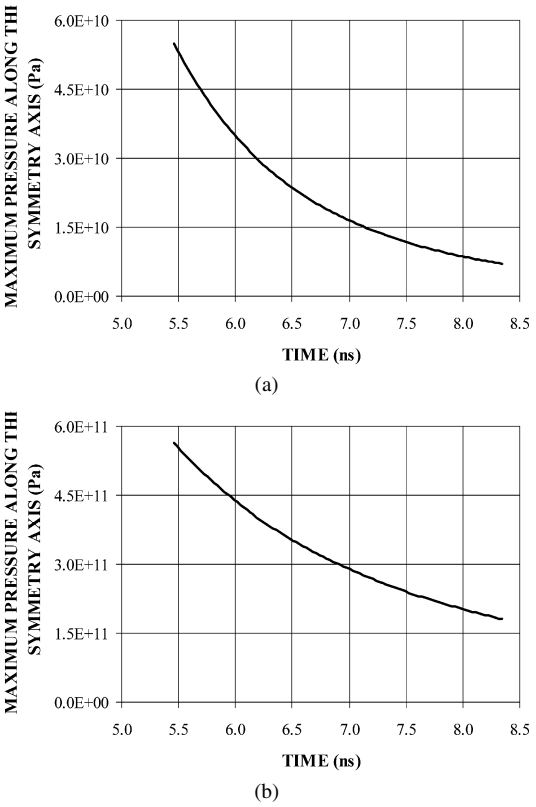

Fig. 12. Temporal variation of maximum pressure along the symmetry axis for two vapor front densities. (a) Vapor front density 800 kg m^{-3}. (b) Vapor front density 50 kg m^{-3}.

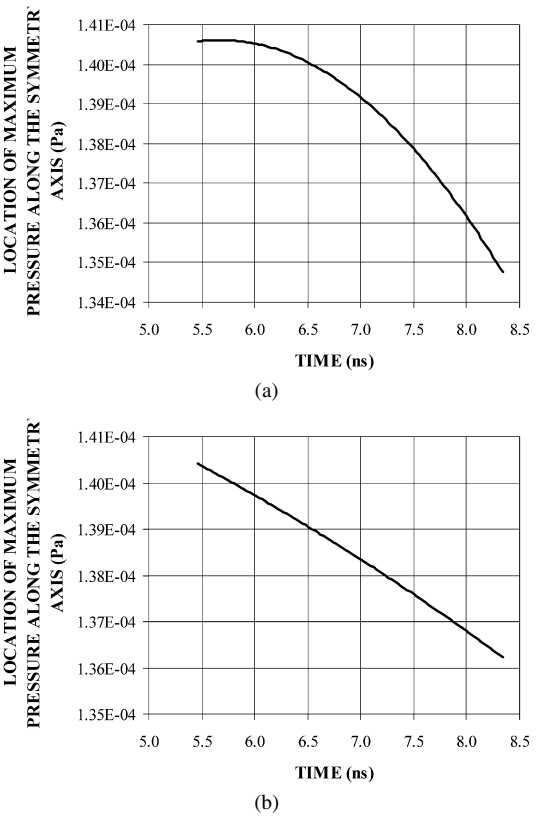

Fig. 13. Temporal variation of location of maximum pressure along symmetry axis for two vapor front densities. (a) Vapor front density 800 kg m^{-3}. (b) Vapor front density 50 kg m^{-3}.

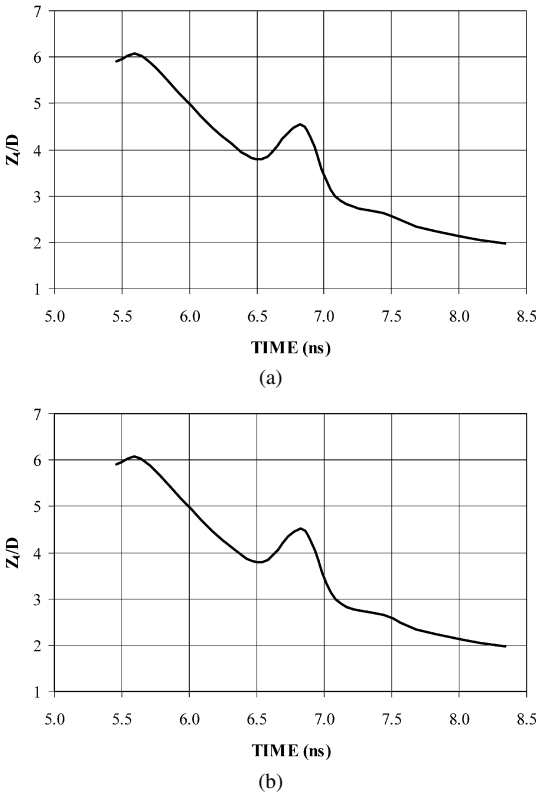

Fig. 14. Temporal variation of jet penetration for two vapor front densities. (a) Vapor front density 800 kg m^{-3}. (b) Vapor front density 50 kg m^{-3}.

mushy zones in the region close to the cavity edge is smaller than that of symmetry axis. The size of solid–liquid mushy zone is smaller than the size of liquid–vapor mushy zone. The jet density has significant influence on the flow structure within and around the expanding jet. Since the mass flow rate emanating from the cavity is kept the same for both densities, jet with low density secures high velocity at cavity exit. This, in turn, results in formation of circulation cell next to the jet boundary immediately after the cavity exit.

The recoil pressure developed in the cavity is considerably high, provided that as the time progresses, it reduces in the vicinity of the cavity due to cavity recession. Since the ambient fluid above the cavity exit has higher density than the jet, it suppresses the axial extension of the jet particularly at long durations. In this case, radial expansion of the jet in the frontal area results in jet neck in the region of the cavity exit. This situation is attributed to the high velocity of the low density jet in the region at the cavity exit. The jet penetration is also influenced by the jet velocity and ambient fluid density. In this case, a local peak in jet penetration occurs due to complex flow structure developed as heating progresses.

Acknowledgements

The authors acknowledge the support of King Fahd University of Petroleum and Minerals, Dhahran, Saudi Arabia for this work.

References

[1] F.W. Dabby, U.C. Paek, High-intensity laser-induced vaporization and explosion of solid material, IEEE J. Quantum Electronics QE-8 (2) (1972) 106–111.
[2] B.S. Yilbas, A. Sahin, R. Davies, Laser heating mechanism including evaporation process initiating the laser drilling, Int. J. Mach. Tools Manufacture 35 (7) (1995) 1047–1062.
[3] P.S. Wei, J.Y. Ho, Energy considerations in high-energy beam drilling, Int. J. Heat Mass Transfer 33 (10) (1990) 2207–2217.
[4] C. Tix, G. Simon, A transport theoretical model of the keyhole plasma in penetration laser welding, J. Phys. D: Appl. Phys. 26 (1993) 2066–2074.
[5] R.K. Ganesh, A. Faghri, Y. Hahn, A generalized thermal modeling for laser drilling process – I. Mathematical modeling and numerical methodology, Int. J. Heat Mass Transfer 40 (14) (1997) 3351–3360.
[6] V. Semak, A. Matsunawa, The role of recoil pressure in energy balance during laser materials processing, J. Phys. D: Appl. Phys. 30 (1997) 2541–2552.
[7] P. Solana, P. Kapadia, J.M. Dowden, P.J. Marsden, An analytical model for the laser drilling of metals with absorption within the vapor, J. Phys. D: Appl. Phys. 32 (1999) 942–952.
[8] B.S. Yilbas, S.Z. Shuja, Laser non-conduction limited heating and prediction of surface recession velocity in relation to drilling, Proc. Instn. Mech. Engrs., Part C: J. Mech. Engrg. Sci. 217 (2003) 1067–1076.
[9] J. Abraham, Entrainment characteristics of transient gas jets, Numer. Heat Transfer, Part A 30 (1996) 347–364.
[10] P. Ouellette, P.G. Hill, Turbulent transient gas injections, J. Fluids Engrg. 122 (2000) 743–753.
[11] H. Kouros, R. Medina, H. Johari, Spreading rate of an unsteady turbulent jet, AIAA Journal 31 (8) (1993) 1524–1526 (Technical notes).
[12] P.O. Witze, H.A. Dwyer, The turbulent radial jet, J. Fluid Mech. 75 (3) (1976) 401–417.
[13] J. Park, H.D. Shin, Experimental investigation of the developing process of an unsteady diffusion flame, Combust. Flame 110 (1997) 67–77.
[14] G.M. Arshad, S.Z. Shuja, B.S. Yilbas, M.O. Budair, Numerical investigation of transient free jet resembling a laser-produced vapor jet, Int. J. Heat Mass Transfer 47 (2004) 1037–1052.
[15] B.S. Yilbas, G.M. Arshad, H.I. Acar, Investigation into laser produced evaporating front characteristics in relation to laser drilling, Lasers Engrg. 13 (1) (2003) 65–74.
[16] B.S. Yilbas, R. Davies, Z. Yilbas, A. Gorur, I. Acar, Surface line and plug flow models governing laser produced vapor from metallic surfaces, Pramana J. Phys. 38 (2) (1992) 195–209.
[17] S.Z. Shuja, B.S. Yilbas, M.O. Budair, Modeling of laser heating of solid substance including assisting gas impingement, Numer. Heat Transfer, Part A 33 (1998) 315–339.
[18] I.Z. Naqavi, Conduction and non-conduction limited laser heating process – mathematical simulation, MSc thesis, Mech. Engrg. Dept., KFUPM, 2001.
[19] S.V. Patankar, Numerical Heat Transfer, McGraw-Hill, New York, 1980.
[20] M. Kalyon, B.S. Yilbas, Analytical solution for laser evaporative heating process: time exponentially decaying pulse case, J. Phys. Part D: Applied Physics 34 (2001) 3303–3311.